Ascent rates of 3D fractures driven by a finite batch of buoyant fluid

Timothy Davis[1]†**, E. Rivata**[2,3] **D. Smittarello**[4] **and R.F. Katz**[1]

[1]Department of Earth Sciences, University of Oxford, South Parks Road, Oxford, OX1 3AN, UK

[2]Dipartimento di Fisica e Astronomia "Augusto Righi", Università di Bologna, Viale Berti Pichat 6/2, Bologna, Italy

[3]GFZ (GeoForschungsZentrum), Physics of Earthquakes and Volcanoes, Potsdam, Germany

[4]European Center for Geodynamics and Seismology, 19 Rue Josy Welter, L-7256 Walferdange, Grand Duchy of Luxembourg

Propagation of fluid-filled fractures by fluid buoyancy is important in a variety of settings, from magmatic dykes and veins to water-filled crevasses in glaciers. Industrial hydro-fracturing utilises fluid-driven fractures to increase the permeability of rock formations; the effect of buoyancy on fracture pathways in this context is typically neglected. Analytical approximations for the buoyant ascent rate facilitate quantitative estimates of buoyant effects. Such analysis exists for two-dimensional fractures, but real fractures are 3D. Here we present novel analysis to predict the buoyant ascent speed of 3D fractures containing a fixed-volume batch of fluid. We provide two estimates of the ascent rate: an upper limit applicable at early time, and an asymptotic estimate (proportional to $t^{-2/3}$) describing how the speed decays at late time. We infer and verify these predictions by comparison with numerical experiments across a range of scales and analogue experiments on liquid oil in solid gelatin. We find the ascent speed is a function of the fluid volume, density, viscosity and the elastic parameters of the host medium. Our approximate solutions can predict the ascent rate of fluid-driven fractures across a broad parameter space, including cases of water injection in shale and magmatic dykes. Our results demonstrate that both dykes and industrial hydro-fractures can ascend by buoyancy over a kilometre within a day.

MSC Codes 74R10: Brittle fracture 76D08: Lubrication theory

1. Introduction

1.1. *Motivation*

Fluid-filled fractures that propagate due to the buoyancy (positive or negative) of the fluid are found in a many geological settings. These fractures are discussed in the literature under various names including gravity-driven hydraulic fractures (e.g Salimzadeh *et al.* 2020), buoyant, liquid-filled cracks (e.g Dahm 2000; Taisne & Tait 2009) and fluid-filled fractures under the influence of weight contrasts (e.g. Pollard & Townsend 2018). Examples of this phenomenon include dykes and veins in the crust, as well as melt-water-filled crevasses in

---

† Email address for correspondence: timothy.davis@earth.ox.ac.uk

36 glaciers. Understanding the rate and extent of propagation of such fractures is critical for
37 making useful, quantitative predictions. For example, the speed with which a batch of magma
38 rises through the crust determines the duration of the warning period between geophysical
39 detection of a dyking event and the volcanic eruption. Fracture ascent speed and distance
40 also have implications for industrial operations. They determine how quickly buoyant fluid
41 can travel away from an injection site, causing potential leakage into critically stressed faults
42 or contaminating the groundwater in overlying geological strata.
43   Field and laboratory observations of fluid-driven fracture provide some indication of
44 typical rates of ascent; for example, in basaltic systems this on the order of mm/s to ~0.5 m/s
45 (Mutch *et al.* 2019; Tolstoy *et al.* 2006). Observations of supraglacial lakes suddenly draining
46 through growing crevasses indicate similar propagation rates (Das *et al.* 2008; Stevens *et al.*
47 2015). Although there is good evidence that water- and gas-filled fractures can ascend through
48 the crust (Schultz 2016; Cartwright *et al.* 2021), this process has not been observed directly.
49 Estimates based on geochemical analysis give ascent rates of ~0.01–0.1 m/s, (1 km/day)
50 (Okamoto & Tsuchiya 2009). Despite these estimates and their relevance for industrial
51 fracking operations, there is a prevailing assumption that buoyant ascent of fluid-filled
52 fractures is negligible or non-existent. This has a direct influence on assessments of the
53 safety of such operations; for examples of this assumption influencing decision-making
54 processes, see the UK and US scientific reviews of hydraulic fracturing safety (Mair *et al.*
55 2012; EPA 2016).

56   1.2. *Previous work and current aims*

57 Analytical predictions of the speed and height of a fracture have previously been obtained
58 from two-dimensional (2D) models. 2D models assume plane-strain elasticity, where there
59 is zero strain out of the plane of interest (x–z) such that the fracture has an infinite extent
60 with invariance along its third dimension (y). 2D models cannot capture effects of the finite
61 lateral extent in y of all real fractures. Nonetheless they provide useful physical insight and
62 can be accurate along a central axis if the fracture is sufficiently broad in the y direction.
63   Two classes of 2D buoyant fractures have been characterised analytically. These are
64 categorised according to the fluid source, either constant area-injection rate or a fixed finite
65 area, where area refers to the volume per unit length in y. Early workers obtained solutions
66 to the problem of a constant injection rate (e.g., Lister & Kerr 1991; Roper & Lister 2007;
67 Rivalta *et al.* 2015). In these studies, injection is along a line-source of infinite length, at a
68 rate that has units of volume per second per distance along the source, $m^2 \, s^{-1}$. At later times,
69 the fracture head ascends buoyantly above a constant-aperture tail, which transmits a steady
70 supply of fluid upward to the head.
71   In the other fluid-source class, Spence & Turcotte (1990) estimated the time-dependent
72 ascent speed of a fixed, finite-area batch of fluid. Unlike the case of constant injection rate,
73 this model predicts a diminishing aperture of the fracture tail, slowing fluid supply to the
74 head, and hence causing the rate of propagation to diminish with time and ascent distance.
75   Analytical approximations for both of these classes have been shown to be consistent with
76 2D numerical solutions (Lister 1990; Roper & Lister 2007; Dontsov & Peirce 2015). The
77 numerics confirm that the elastic constants and material toughness influence the shape of the
78 propagating head but not the ascent speed. The latter is determined by the width of the tail.
79   Three-dimensional (3D) fractures, with finite extent in the y direction, pose additional
80 challenges to analysis. Workers have begun to investigate the case of constant volume injection
81 rate in 3D (Möri & Lecampion 2021*b*), proving approximate analytical solutions for the height
82 as a function of time, the width and the aperture of the fracture. In contrast, there there has
83 been no analysis of the ascent speed of a 3D fracture containing a fixed volume of fluid. And
84 yet such analysis would be valuable in various contexts. In volcanology, where the volume

of intrusions is often well-constrained by geodetic data, a 3D solution would help to estimate parameters that drive dyke ascent through the crust; it would enable rapid assessment of the likelihood of eruption. In industrial operations, both the source rock properties and volumes of fluid injected are well constrained, but currently there is no simple way of predicting how fast an injected batch of fluid will ascend by buoyancy.

Here we develop an analytical solution that predicts the size and ascent speed of a 3D fracture driven by a finite volume of buoyant fluid. In developing this solution, our first aim is to provide an upper bound on the ascent speed of fractures that are propagating due to the buoyancy of a finite batch of fluid. Our second aim is to understand how this ascent speed decays with time, as in the 2D solution of Spence & Turcotte (1990).

Our strategy is to use a state-of-the-art numerical simulator (Zia & Lecampion 2020) to produce 3D solutions to the full, non-linear equations. We treat these as a benchmark for our novel analytical results, to show their applicability. The manuscript is organised as follows. In the next section we review existing analytical approximations and introduce the simulator of Zia & Lecampion (2020). We use this to simulate the ascent of a fixed finite-volume fluid batch, reviewing this simulation in detail to describe the problem. In section 3, we use these insights and proceed to derive equations describing the ascent speed of a 3D, finite batch of fluid. In section 4, we use 3D simulators to test the validity of these results across a range of scales. We then test the ability of our approximations to predict the ascent speed of oil-filled cracks in gelatin solids. Lastly, in Sec. 5, we discuss the implications of our results in relation to selected case studies, detailing limitations and potential avenues of future research.

2. Background

In this section we first review approximate analytical solutions for two- and three-dimensional fractures, then consider numerical simulators that solve the full, non-linear problem.

2.1. *Analytical solutions*

2.1.1. *Critical lengths and volumes*

A fluid-filled fracture will either ascend or descend, depending on the density of the fluid relative to that of the surrounding solid medium. This has been well documented in analog experiments by comparing, for example, the injection of air and mercury into gelatin solids as described in Heimpel & Olson (1994). For simplicity here, we consider only positively buoyant (less dense) fluids, and hence we model only fracture ascent, noting that there is no loss of generality in the solutions derived.

Fluid-filled fractures are driven to ascend by a weight contrast $\Delta\gamma$ between the fluid and surrounding rock. More specifically, the buoyancy force is defined as the difference between the vertical gradient of the horizontal stress in the rock column and the volume-specific weight of the magma contained within a vertical fracture. Assuming the horizontal and vertical stresses are equal, i.e., a lithostatic state of stress, then $\Delta\gamma = (\rho_r - \rho_f)g$ (Secor & Pollard 1975), where ρ_r and ρ_f are rock and fluid density, respectively, and g is the acceleration due to gravity.

Weertman (1971) and Secor & Pollard (1975) showed that fluid-filled fractures can ascend through their solid host by hydraulic fracturing, provided a critical areal extent A_c is exceeded,

$$A_c = \frac{(1-\nu)}{2\mu} \frac{K_c^2}{\Delta\gamma}. \tag{2.1}$$

Here the stress intensity factor K_I appears as K_c to represent the fracture toughness of the host rock for mode-I fracture (Tada *et al.* 2000). This is derived by requiring that the fracture

129 walls close shut at the lower tip ($K_I(z = -c) = 0$) and that the upper tip is critically stressed
130 ($K_I(z = +c) = K_c$), where c is the fracture's half-length and z the vertical distance from
131 its centre (Pollard & Townsend 2018). Working independently, Dahm (2000); Salimzadeh
132 *et al.* (2020); Davis *et al.* (2020); Smittarello *et al.* (2021); Möri & Lecampion (2021*b*) each
133 extended the 2D analytical model of Secor & Pollard (1975) to quantify the critical volume
134 of fluid for ascent of a 3D fracture. The solutions derived in these studies have the same
135 scaling with parameters but differ by around 10% because of different numerical constants.
136 The solution for critical volume by Davis *et al.* (2020) is

$$V_c = \frac{(1 - \nu)}{16\mu} \left(\frac{9\pi^4 K_c^8}{\Delta\gamma^5} \right)^{1/3}, \qquad (2.2)$$

138 where ν and μ are Poisson's ratio and the shear modulus of the host rock, respectively. When
139 the volume of fluid in a fracture exceeds V_c, the ascent of the fracture and contained fluid
140 is self-sustaining. By this we mean that the ascent is due to buoyancy alone, and requires
141 no additional forces such as a driving pressure (e.g., from a pressurised magma chamber or
142 well bore). As the fracture ascends, the tail of the crack lengthens and thins, but the fracture
143 head retains a volume sufficient to critically stress the medium ahead of it. Figure 1 shows
144 numerical solutions, discussed below, that illustrate this.

2.1.2. *Ascent rate*

146 Results cited above quantify the critical conditions for buoyant ascent, but not the speed of
147 that ascent. The latter requires a consideration of the fluid flow within the fracture. In the tail
148 of the fracture this can be usefully approximated as Poiseuille flow between parallel plates.
149 At small Reynolds number, lubrication theory gives the mean flow speed v and areal flux Q
150 as

$$v = \frac{w^2}{12\eta}\Delta\gamma, \qquad Q = \frac{w^3}{12\eta}\Delta\gamma, \qquad (2.3)$$

152 where w the separation of the plates, η is the dynamic viscosity and we have assumed that
153 the gravity vector is parallel to the walls. Here it is assumed that the fluid flow between the
154 fracture's walls is laminar.
155 The ascent rate of a 2D fracture with constant areal flux Q is given by eliminating w from
156 equations (2.3) to give (Lister & Kerr 1991)

$$v_Q = \left(\frac{Q^2\Delta\gamma}{12\eta} \right)^{1/3}. \qquad (2.4)$$

158 This result means that for Q constant, the speed of the upper tip is controlled by viscous flow
159 through a tail of constant width, which transports buoyant fluid upward to the propagating
160 head.
161 The ascent rate of a 2D fracture with constant area A is given by combining (2.3) with a
162 conservation of mass equation that relates the rate of change of aperture to the divergence of
163 the vertical flux (Spence & Turcotte 1990). On this basis, Spence & Turcotte (1990) obtained
164 a solution in terms of the velocity of flow through a half-ellipse with a fixed area. As this
165 lengthens vertically its aperture decreases, which hinders fluid flow and slows the ascent of
166 the fracture tip. The rate at which the half-ellipse lengthens therefore progressively decreases
167 with time. Differentiating with respect to time equation (22) of Spence & Turcotte (1990),
168 which defines the z distance between the upper tip and the initial centre-point of the fracture

169   (the injection point), the fracture's tip velocity is

170
$$v_A(t) = \left(\frac{A^2 \Delta \gamma}{48\eta}\right)^{1/3} t^{-2/3}. \tag{2.5}$$

171   The ascent rate of a 3D fracture with a constant rate of volume injection was considered
172   by Lister (1990). His equation (2.14) provides an approximate 3D scaling for fracture height,
173   breadth and aperture at a given injection rate (see also Germanovich *et al.* 2014). These
174   scalings have been confirmed by Möri *et al.* (2020) and Möri & Lecampion (2021*b*) using
175   3D numerical simulations computed with open-source codes (Zia & Lecampion 2020;
176   Salimzadeh *et al.* 2020). Möri *et al.* (2020) and Möri & Lecampion (2021*b*) show that
177   for a 3D, constant injection-rate, ascending fracture, the shape of the tip-line depends
178   on a dimensionless ratio that includes viscosity and fracture toughness. Close to the
179   injection point, viscous resistance limits tip-line propagation, resulting in a V-shaped tip
180   line; sufficiently far from the injection point, fracture toughness limits tip-line propagation
181   and the tip-line at either side of the fracture is vertical. These limiting regimes correspond
182   with the asymptotic solutions for aperture near the tip-line (Detournay 2004).
183   The ascent rate of a 3D fracture containing a constant volume of fluid is not known.

2.2. *Numerical Methods*

185   We run 3D simulations of an ascending fluid batch with a constant-volume using a
186   hydro-fracture simulator. This 3D simulator generates numerical solutions to the nonlinear
187   governing equations. These solutions guide the development of our approximate analysis
188   for constant-volume fractures. Comparison of our analytical and numerical solutions then
189   enables us to determine the validity of simplifying assumptions and assess the accuracy of
190   our analytical predictions.
191   We simulate the propagation of buoyancy-driven fractures using the open source code
192   PyFrac (Version 1.0, https://pyfrac.epfl.ch). PyFrac's methods and implementation
193   are extensively documented in Zia & Lecampion (2020). The calculations we present use the
194   code as described in that original work, and hence we only summarise the algorithm here to
195   give a sense of its aptitude for solving hydro-fracture problems.
196   The hydro-fracture problem comprises three coupled physical aspects: fluid flow and
197   pressure inside the fracture, deformation of the surrounding medium due to the fracture,
198   and propagation of the fracture's tip-line into the unfractured medium. These aspects are
199   independently modelled as low Reynolds-number fluid flow, quasi-static linear elasticity, and
200   linear-elastic fracture mechanics, respectively. Although each is linear independently, their
201   coupling results in a non-linear equation system. The time-dependent solution to this system
202   is the location of the tip-line, the fracture aperture, and the fluid pressure and velocity. The
203   PyFrac solver limits the complexity of this problem by restricting solutions to be planar
204   fractures. This simplification enables pre-computation of the Green's functions required
205   for the Displacement Discontinuity Method (DDM) using a fixed-grid mesh (Peirce 2016).
206   The DDM method links fluid pressure inside the fracture to the opening of its walls and
207   to deformation of the surrounding medium. On the same mesh, the lubrication equation is
208   discretised using the finite volume method at element centres. The gradients in fluid pressure
209   determine the rate of flow between cells. Crucially, to avoid the requirement of ultra-high mesh
210   resolution near the fracture tip, the PyFrac uses near-tip asymptotic solutions for propagating,
211   fluid-filled fractures. These asymptotic solutions resolve the sub-grid-scale dynamics, and
212   hence are used to assess the propagation criterion and rate of tip-line motion. By comparison
213   of numerical solutions to existing analytical solutions (Peirce 2015, 2016; Zia *et al.* 2018;

214 Zia & Lecampion 2020; Moukhtari *et al.* 2020), it has been shown that PyFrac can accurately
215 solve the coupled hydro-fracture growth problem.
216   For simulations in the present manuscript the extent of the meshed domain in the horizontal
217 direction is $2a$, the characteristic radius we define below. The vertical extent of the domain is
218 sufficient to capture propagation of the fracture in the post-injection, buoyancy-driven regime
219 without re-meshing ($14a$). Along the horizontal direction we use a minimum grid size of 50
220 elements, the vertical grid is created such that the elements are square. We remind readers
221 the meshed domain is only used to discretise the fracture itself. Displacements and stresses
222 due to the fracture are described by Green's functions for an infinite space such that these
223 hold anywhere in the body. Injection of the fluid occurs from a point source.

2.3. *Qualitative insights from numerical simulations of fracture ascent*

225 Using the numerical method described above, we simulate the injection of a finite batch of
226 buoyant fluid, closely following a case that was analysed by Salimzadeh *et al.* (2020). The
227 parameter values for this simulation are provided in Table 1.
228   In Fig. 1 we plot snapshots of the fracture's shape as it evolves thorough time. Time
229 increases from left to right in the plot. Looking onto the fracture's face, soon after the
230 injection has ceased (10 minutes), the fracture's tip-line is circular. Note the asymmetric
231 aperture of the cross-section at this time, which indicates that the fluid is starting to flow
232 towards in the upper tip of the fracture. After 6 hours the top of the fracture has grown
233 upwards whilst the tip-line in lower region has not changed shape; when looking at the
234 face at this stage, the tip-line on either side of the fracture tapers progressively towards the
235 top. The form of the upper part of the tip-line is a semi-circle and remains so throughout
236 the rest of the simulation. As time increases the aperture in the lower parts of the fracture
237 progressively thins. 6 hours into the simulation, the fracture has reached a characteristic
238 shape; in cross-section, the lower half of the fracture (tail) is thin and V-shaped while the
239 upper half (head) has formed the teardrop profile of a Weertman crack (Roper & Lister 2007).
240 Looking onto to the face at 15 hours, the fracture's upper tip has continued to rise, resulting
241 in a tip-line on either side of the fracture that is approximately vertical, where the tapering
242 upwards is less evident. The cross-sectional aperture retains the typical structure predicted by
243 2D analytical solutions, with a clearly defined teardrop-shaped head and tapered tail (Roper
244 & Lister 2007). This structure dominates at late times ($t>15$ hours), noting the thinning of
245 the tail as the length increases, whilst the head's shape remains roughly constant.
246   In Fig. 2a we plot the speed of the upper-most point on the fracture's tip-line as a function
247 of time (log scale). We refer to this speed as the ascent rate because it is identical to the
248 speed at which the head of the fracture rises through the medium. A dashed line showing
249 $t^{-2/3}$ from equation (2.5) is overlain. At late-times > 6 hrs, the velocity of the 3D numerical
250 solution approaches the $t^{-2/3}$ asymptote described by the 2D analytical solution.
251   In Figure 2b we plot the ascent rate as a function of the height of the fracture. Note the
252 y-axis has a logarithmic scale and the times shown in Fig. 1 are plotted as asterisks. In the
253 later stages of the simulation, the ascent rate has undulations that repeat every few iterations
254 of the simulation; we interpret these as being are due to numerical instability. The undulations
255 have a roughly uniform magnitude that depends on the mesh size. Neglecting these, the plot
256 shows two clear changes in front deceleration. The first occurs once the injection stops (Möri
257 & Lecampion 2021a), and the second once the upper tip has propagated further than $2a$,
258 a characteristic radius we examine later. We interpret the second transition in the ascent
259 speed to a shift in the process driving tip-line growth, from a radial injection-rate-driven
260 fracture growth to buoyancy-driven fracturing, occurring once the upper tip of the fracture
261 has propagated a given distance. If this interpretation is correct then at later times the decay
262 in ascent speed should be related to the fluid draining upward from the increasingly long

Quantity	Symbol	Unit	Value
Young's modulus	E	Pa	20×10^9
Poisson's ratio	ν		0.25
Fracture toughness	K_c	Pa m$^{1/2}$	2.0×10^6
Fluid/rock density difference	$\Delta \gamma$	kg m^{-3}	1000
Fluid viscosity	η	Pa s	0.05
Injected Volume	V_I	m^3	1.95
Critical Volume	V_c	m^3	0.79
Volume ratio	V_I/V_c		2.47
Injection rate	$Q(t)$	m^3 s^{-1}	0.015

Table 1: Parameter values used for the simulation shown in Figs. 1 & 2. These correspond to simulation-case II from the main text of Salimzadeh *et al.* (2020).

and thin tail (Eq.2.5) (Spence & Turcotte 1990). Such a thinning of the tail aperture can be seen in the snapshots of the ascending fracture in Fig. 1. In the following section we provide analytical expressions approximating: (i) the fracture's maximum lateral extent a (Fig. 1), (ii) the maximal upwards propagation speed once injection has terminated (dashed line in Fig. 2b)), and (iii) the deceleration of the ascending fracture with time (Fig. 2a).
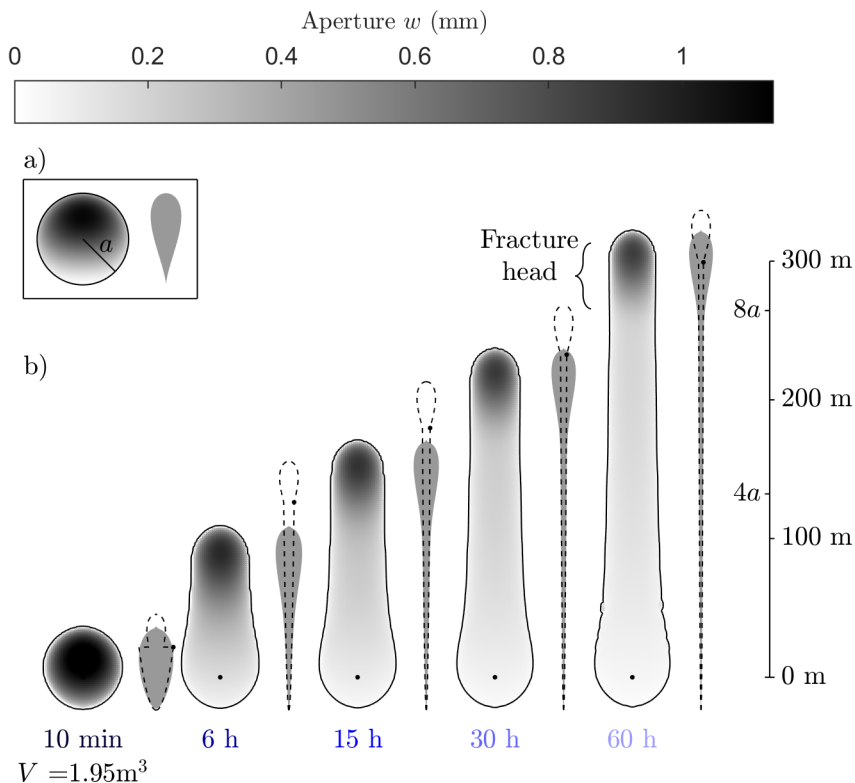
Figure 1: Numerical simulation of an ascending finite fluid batch. In this simulation 1.95 m^3 of fluid was injected over 130 seconds. Two views of the fracture are shown at each time. On the left is a view looking onto the fracture's face, shaded by aperture (w) with the tip-line in black. On the right is a grey cross-section showing the profile of aperture along the centre of the crack. The latter has a horizontal exaggeration of 2×10^4.
a) Analytical solution that defines the radius a. The plotted solution contains fluid volume V and has a radius such that $K_I(z = -a) = 0$.
b) Numerical simulation of fracture ascent using PyFrac (Table. 1). Simulation times are shown below the respective fractures. The time dependant analytical approximation of the fracture's cross-section is shown as dashed lines (Roper & Lister 2007). The tail height h (3.5) is marked with a dot.
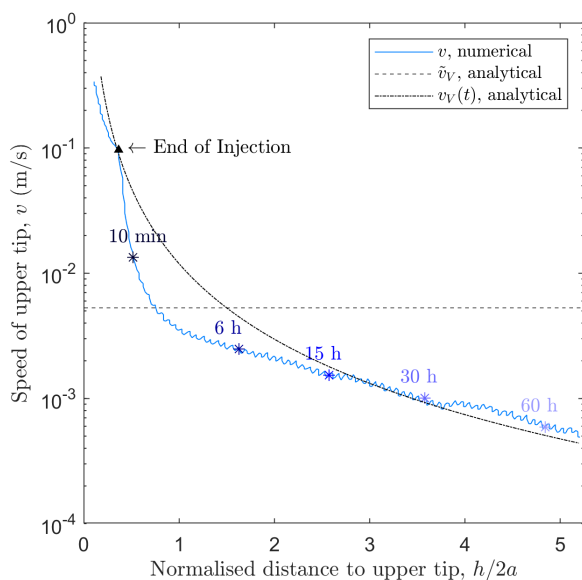
a)
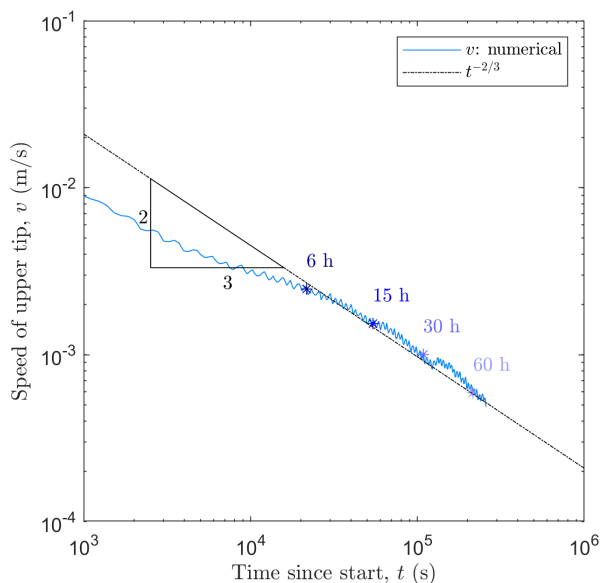
b)

Figure 2: Upper tip ascent speed from PyFrac simulation (solid line) and analytical approximations (broken lines). Times corresponding to steps in Fig.1 are shown as asterisks. Parameter values are given in table 1. *a)* Ascent rate versus time, log-log plot showing that at late-times the simulations approach the $t^{-2/3}$ asymptote (dash-dot). *b)* Ascent rate versus height, showing our equation for the maximum ascent speed (3.4) as a horizontal dashed line, and the analytical approximation of the decelerating front speed produced using equation (3.5) for *x* values and (3.6) for *y* values (dash-dot line).

3. Analysis of three-dimensional fracture ascent rates

3.1. *Early-time ascent rate*

As a first pass, we aim to approximate the ascent rate of a buoyancy-driven fracture at an early time. Here we refer to the moment after injection when ascent becomes dominantly driven by buoyancy. This moment does not occur precisely at the end of injection; some ascent beyond that time is driven by the release of elastic energy stored during the injection phase, which drives a radial motion of the tip line (Möri & Lecampion 2021*a*). This energy is expended rapidly, after which buoyancy dominates in driving ascent. Our first calculation is an estimate of the speed of ascent at this point.

We assume that a volume V of fluid has been injected and resulted in a penny-shaped crack. The crack has extended radially to a size such that the deepest segment of the tip line, the bottom tip, has ceased its radial advance. The walls of the crack are subject to a downward stress gradient of magnitude $\Delta\gamma$ that drives fluid upward. As this gradient becomes dominant post-injection, the fracture above the bottom tip begins to drain fluid and pinch closed.

Injection of a volume V leads to a penny-shaped crack with mean internal pressure given by

$$p_0 = \frac{3\mu}{8(1-\nu)}\frac{V}{a^3},\tag{3.1}$$

where a is the radius of the tip-line around the injection point (Tada *et al.* 2000). The mode-I stress intensity at the circular tip line arises from a combination of p_0 and the linear stress gradient (Tada *et al.* 2000),

$$K_I(\theta) = \frac{2}{\pi}\sqrt{\pi a}\left(p_0 + \frac{2}{3}\Delta\gamma a \cos(\theta)\right),\tag{3.2}$$

where θ is the angle in the y-z plane away from vertical. If z is the upward distance from the injection point, eliminating the mean pressure from equations (3.1) and (3.2) and requiring that at the basal tip $K_I(z=-a)=0$ gives the radius of the crack as

$$a = \left(\frac{9\mu}{16(1-\nu)}\frac{V}{\Delta\gamma}\right)^{1/4}.\tag{3.3}$$

The mean aperture of this crack is simply given by $w = V/\pi a^2$; using this in (2.3) to compute the characteristic fluid ascent speed v, then combining the result with (3.3) to eliminate a we obtain

$$\tilde{v}_V = \frac{4(1-\nu)}{27\pi^2\mu}\frac{\Delta\gamma^2 V}{\eta}\quad\text{for }V > V_c.\tag{3.4}$$

Here we have assumed that the fluid ascent speed v is equal to the speed of the upper tip line $\tilde{v}_V$ (the tilde indicates that this is an early-time solution and the subscript V indicates that this is a fixed-volume, 3D fracture). This speed is plotted as a horizontal dashed line in Figure 2b.

Equation (3.4) is the speed of the upper tip when the crack is still penny-shaped, just after the phase of radial growth driven by the injection. As the upper tip propagates driven by buoyancy of the fluid, the crack elongates vertically. The stress gradient drives fluid within the crack upward such that part of the total fluid volume V resides in the head the crack, while the remainder forms a slowly thinning layer in the long tail (Fig. 1). Thus, equation (3.4), which describes the instant when the entire fluid volume is in the head, gives an approximate upper bound on the buoyancy-driven ascent speed.

3.2. *Finite propagation with deceleration*

We now consider the vertical advance of the fracture over finite time. We define h as the vertical distance between the fracture's upper tip and the initial centre of the crack (the injection point). Recalling that Fig.2a shows that the ascent rate of the 3D simulation asymptotically scales with time as predicted by equation (2.5), this motivates us to approximate the 3D ascent speed using this 2D solution. To retrieve $h(t)$ and $v(t)$ for our 3D fracture, we modify the similarity solution obtained by Spence & Turcotte (1990, eq. 22) for a 2D fracture with constant area. Replacing that area A with the initial cross-sectional area of the 3D crack $2aw$ gives

$$h = \left(\frac{9\,(2aw)^2\,\Delta\gamma t}{16\eta} \right)^{1/3}. \tag{3.5}$$

Substituting equation (3.3) and $w = V/\pi a^2$ into (3.5) and defining the speed $v_V(t) \equiv \mathrm{d}h/\mathrm{d}t$,

$$v_V(t) = \left(\frac{(1-\nu)}{9^2\pi^4\mu} \frac{\Delta\gamma^3 V^3}{\eta^2} \right)^{1/6} t^{-2/3}. \tag{3.6}$$

This approximate solution might be expected to hold at later times, when buoyancy has driven the fracture to propagate away from the injection point, establishing distinct tail and head regions of the fracture. Assuming that this structure is in place once the upper tip has advanced to a height $h = 2a$, we use (3.5) to define late time as $t > t_r$ where

$$t_r = \left(\frac{3^2\pi^8\mu^5}{(1-\nu)^5} \frac{\eta^4}{\Delta\gamma^9 V^3} \right)^{1/4}. \tag{3.7}$$

Figure 2b shows the predicted initial and late-time speeds from equations (3.4) and (3.6), respectively. The figure also shows a numerical solution of a 3D crack for the same parameter values. The ascent rate predicted by (3.6) at $h = 2a$ (corresponding to $t = t_r$) is greater than the numerical result at the same position; at this point, the early-time approximation (3.4) fits better. At $h/2a = 3/2$, the two approximations are equal $\tilde{v}_V = v_V(t)$. As the fracture ascends beyond this height, the full, numerical solution and the late-time solution converge. This convergence was also obtained in 2D numerical solutions by Roper & Lister (2007, Fig. 9).

3.3. *Comparison between the numerical results and analytical predictions*

Using the initial cross-sectional area $2aw$ noted above, we plot as dashed lines in Fig. 1 the cross-section predicted by the 2D similarity solutions of Roper & Lister (2007, Sec. 6) (Also see our Appendix A). The height of the tail in these cross-sections is given by equation (3.5). Focusing attention on the solutions at elapsed time of 30 hours, the analytical solution provides a good fit to the width of the tail from the numerical solution. Furthermore, the simulated fracture's head length and shape are approximately that of the Weertman solution. The notable discrepancy is that analytical solution predicts a greater propagation distance than produced by the simulation. This discrepancy is also evident in the comparison of fracture ascent speeds of Fig. 2b where, initially, the analytical prediction is for faster propagation, but as the simulation progresses and the fracture lengthens, the numerical and analytical speeds converge. Next we discuss the assumptions made in the derivation of (3.6) to explain why the numerical and analytical ascent rates and heights differ.

We begin with a reminder of three insights from 2D results by Roper & Lister (2007) that also apply here. Firstly, as long as the cross-sectional area of the initial 2D crack is above the critical head area given by equation (2.1), the fracture is predicted to ascend indefinitely, with a monotonically decreasing propagation rate. Secondly, in the 2D, constant-area theory,

elastic forces dominate in the head region, resulting in a head shape that remains constant over time and is described by the static Weertman solution (Weertman 1971; Rubin 1995). Thirdly, Roper & Lister (2007) show that the area of the head should be removed from the total area when computing the dynamics of the tail (e.g., (3.5)) and, in particular, in estimating the velocity and height of the fracture.

Keeping these insights in mind, we next evaluate assumptions of the 2D, constant-area approximate solution to observations from our 3D simulation from Fig. 1. In the 2D solution, the areal extent of the head is constant during ascent, whereas in the 3D simulation, the effective head volume decreases with time. This is qualitatively shown by the lateral tip-lines in Fig. 1 that slightly converge upwards over time. Because of this feature, we have neglected to approximate the head volume, placing the entire cross-sectional area of the initial penny-shaped crack into the tail solution. Our analytical result is therefore based on an overestimate of the tail volume, and hence it should predict a faster ascent rate than the numerical simulation. This explains why initially, the predicted velocities are faster. Moreover, in the 2D solution (3.5), the cross-sectional area of the fluid (tail plus head) is constant. This contrasts with observations in the simulation shown in Fig. 1 where along the centreline, the fracture's cross-sectional area increases by 36% from the earliest (10 minutes) to the latest (60 hours) snapshots. This out-of-plane fluid flow is, by definition, not captured by the 2D solution. Thickening of the cross-section in the 3D simulation suggests that the ascent rate for a 3D fracture will be faster than its 2D analogue at later times.

3.3.1. *Turbulent flow*

Up to this point, we have assumed that the crack aperture is small and that the viscosity is large enough that a lubrication approximation can be applied to the flow. To test this assumption of laminar flow, the Reynolds number can be computed using

$$\mathrm{Re} = \frac{w v \rho_f}{\eta}, \tag{3.8}$$

where, as a first approximation, crack aperture w can be obtained according to $w = V/\pi a^2$ and v can be taken as the initial buoyancy-driven ascent rate from equation (3.4). For flow between parallel plates, Reynolds numbers larger than $\sim$1400 are associated with turbulence. Here we avoid empirical formulations describing flow speeds in turbulent regimes for the sake of simplicity, focusing instead on the upper limit of the ascent speed that is described by laminar flow.

For analog experiments using air-filled cracks in gelatine, (e.g. Heimpel & Olson (1994), Smittarello *et al.* (2021)), equation (3.4) vastly overestimates measurements of the crack ascent rate. For example, assessing the Reynolds number for an air-filled crack in a gelatin solid with a stiffness E of 1500 Pa, toughness K_c of 50 Pa m$^{1/2}$ and a volume calculated from equation (2.2), we find that is is greater than 2900, and hence turbulent flow is expected and may account for the slow ascent.

Quantity	Symbol	Unit	Oil in gelatin	Water in shale	Basaltic dyke
Shear modulus	μ	Pa	276	8×10^9	25×10^9
Poisson's ratio	ν		0.25	0.25	0.25
Fracture toughness	K_c	Pa m$^{1/2}$	19	2.0×10^6	6.0×10^6
Fluid/solid density difference	$\Delta\gamma$	kg m^{-3}	160	2,000	50
Fluid viscosity	η	Pa s	4.8×10^{-2}	5×10^{-3}	20
Critical Volume (2.2)	V_c	m^3	1.31×10^{-5}	0.7921	700

Table 2: Properties used to numerically simulate fracture ascent for different physical processes. The injection rate for such cracks is set to $(V/\bar{v}_V)/a$, such that the injection is complete before the fracture ascends past $h = 2a$.

4. Validation of analytical approximations

4.1. *Testing across length scales by comparison to numerical solutions*

We now test our analytical approximations against numerical solutions across a wider range of physical parameters. Here, each parameter set represents a different physical context: analog experiments with oil-filled cracks in gelatin, an industrial setting where water is injected into a shale sequence and, lastly, the ascent of a basaltic dyke through the crust (Table 2). We compare our analytical prediction from equation (3.6) against rates obtained from PyFrac calculations using the three parametric combinations listed in Table 2, each of which is simulated for three different injection volumes to give nine total models. Results are shown in Figure 3, in comparison with analytically predicted rates. The comparison shows that $v_V(t)$ from (3.6) provides a reasonable match to the numerical results across all parameter sets considered. The undulations in propagation speed from PyFrac are again clear in this plot, and again we attribute these to numerical instability. Ignoring them, the analytical results predict the PyFrac velocities within a factor of two. The ratio of numerical to analytical ascent speed is approximately constant for a given simulation. In Figure 4, we compare our analysis (3.5) to numerical results in terms of the time-dependent height of the upper tip above the injection point. As in the previous figures, we find the fracture must ascend by a length of more than $2a$ (box shown is $3a$) before buoyancy becomes the dominant driver of propagation. After that time, the results show the predicted and simulated heights are comparable. These comparisons show that our analytical approximations capture the leading-order fracture ascent speed across a broad parameter space. We further note that our analytical results for the extent and ascent speed provide a reliable means to forecast the required PyFrac domain size and simulation duration for a given set of parameters, such that the numerical model converges and completes the intended simulation.
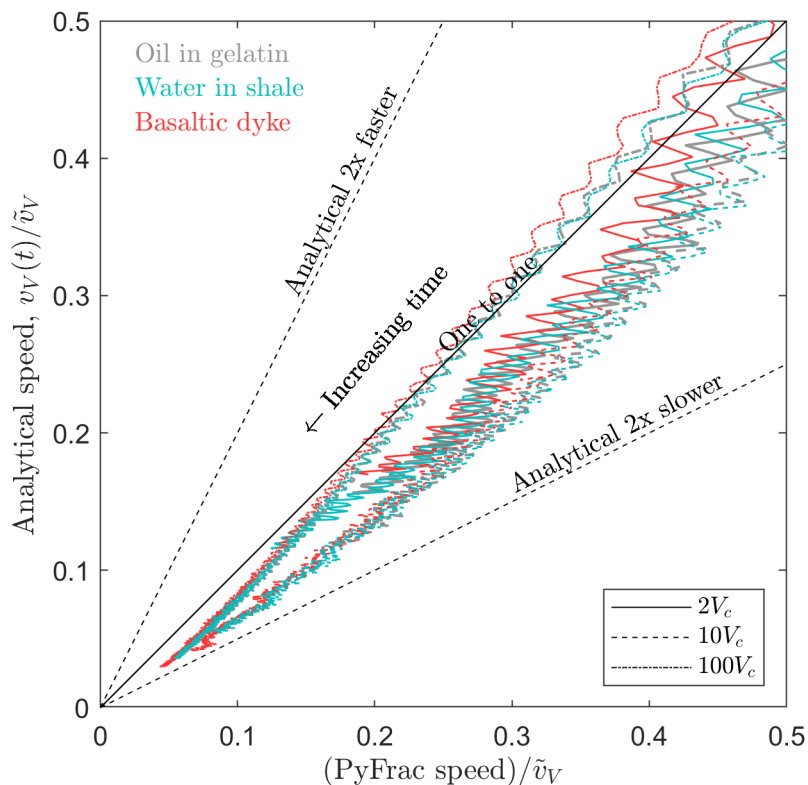
Figure 3: Numerical versus analytical (3.6) speed estimates at times *t* since injection. Plotted are nine simulations performed using the code of Zia & Lecampion (2020) and summarised in Table 2. These comprise three parametric cases, each with three different injection volumes and rates. The plots stop at the point when the simulated fracture reached the edge of the meshed domain or Pyfrac terminated the simulation.
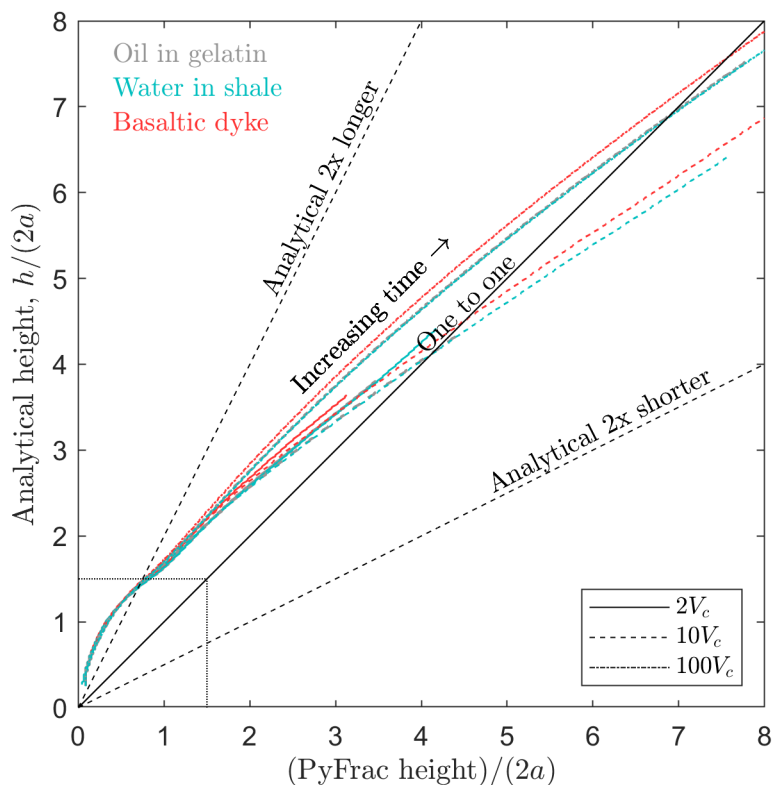
Figure 4: Numerical versus analytical (3.5) height estimates at times t since injection. Height here is defined as the distance from the injection point to the upper tip. This plot uses the same numerical solutions as in Fig. 3.

Quantity	Symbol	Unit	Exp. 1933	Exp. 1945	Exp. 1967
Young's modulus	E	Pa	1995	306	595
Poisson's ratio	ν		0.5	0.5	0.5
Fracture toughness	K_c	Pa m$^{1/2}$		17	23.8
Oil/gelatin density difference	$\Delta\gamma$	kg m^{-3}	260	160	150
Oil viscosity	η	Pa s	1.74×10^{-3}	48×10^{-3}	970×10^{-3}
Injected Volume	V_I	m^3	40	10	10
Critical Volume (2.2)	V_c	m^3		2.64×10^{-5}	3.72×10^{-5}
Predicted velocity (3.4)	$\tilde{v}_V$	m s^{-1}	1.69	0.038	8.4×10^{-4}
Reynolds number (3.8)	Re		3.1×10^3	2.81	0.0022

Table 3: Properties of the analog gelatin experiments of Smittarello (2019). Experiment reference numbers are shown in the first row. Note that the injection rates were not recorded.

### 4.2. *Comparison to analog oil injection gelatin experiments*

The gelatin experiments of Heimpel & Olson (1994) and Smittarello (2019) show that crack ascent rates are related to the injected volume. Our analysis can be used to understand what determines the speed of fractures in such experiments. We reiterate that our predicted maximum ascent speed (3.4) is an overestimate for cracks filled with low-viscosity fluids, such as air, that are prone to turbulence (as is the case in many analog experiments). The Reynolds number in (3.8) can be used to assess whether the flow in the fracture is turbulent, which we have shown is generally true for gelatin experiments with air-filled fractures. Additionally, many fluids typically injected such as air and water, are non-wetting fluids when in contact with gelatin solids. When these flow through fractures in gelatin, the lubrication approximation breaks down; all fluid can be expelled from between the walls. Both effective closure of the fracture's tail and near-constant ascent rates are indications that non-wetting processes are active. This has led some authors to conclude that typical experimental fluids are not a good analog for the fluids that drive fracture in the crust (Taisne & Tait 2009).

Silicon oils are wetting with respect to the gelatin. In Fig. 5 we plot the speed of silicon oils hydro-fracturing upward through gelatin solids. The experiments are described in Smittarello (2019); the material properties are given in Table 3. These experiments have well-constrained injection volumes and elastic parameters, and therefore provide a suitable basis for comparison with our equations.

Figure 5a shows that after the post-injection transient ends, the ascent speed of the experimental fractures follow the $t^{-2/3}$ trend. Fig. 5b shows that our analysis predicts the rate of upward propagation in the buoyancy-driven regime within a factor of two of the observed speed. This good match appears to be independent of the rate of injection, presence of tank walls and free surface, loads placed on the gelatin during the experiments and the evolving elastic properties during the time span of the experiments as the gelatin warms (Smittarello 2019). Note that the fracture accelerates as it approaches the free surface. In Fig. 5a, this appears as a deviation from $t^{-2/3}$ trend toward reduced deceleration at later times (Rivalta & Dahm 2006). The line representing experiment 1933, where the prediction is off by an order of magnitude, shows the effect of a high Reynolds number (Table 3), which significantly reduces the ascent speed of the fracture relative to that predicted by laminar flow.
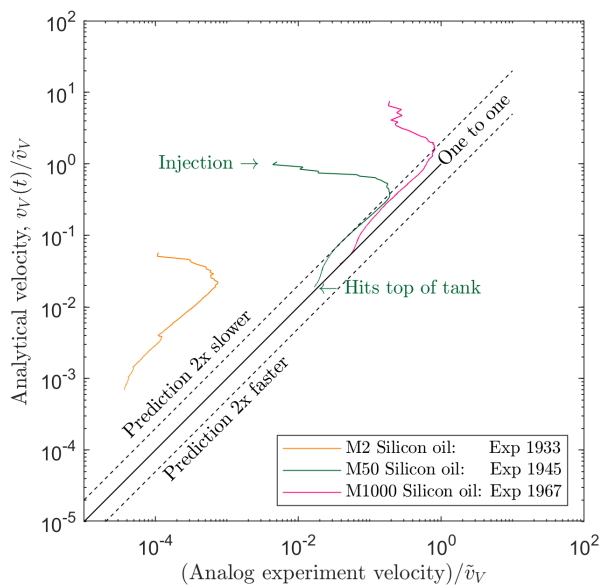
a)
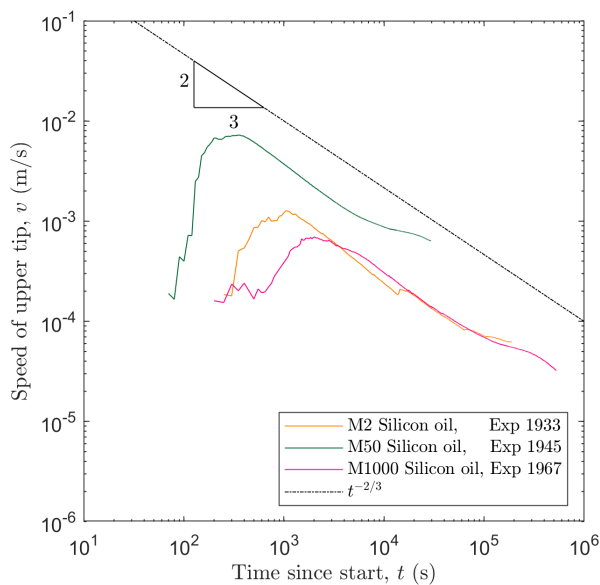
b)

Figure 5: Upper tip ascent speed from analog experiments where silicon oil is injected into in gelatin solids. Parameter values are given in table 3. *a)* Ascent rate versus time, showing that at late times, curves approach the $t^{-2/3}$ asymptote (dash-dot). *b)* The speed from the experiments is plotted against the predicted speed using equation (3.6), where the time is that elapsed since the start of the injection.

5. Discussion

5.1. *Some insights into ascent velocity*

In our numerical simulations, we have made sure that the injection rates are such that the specified fluid volume has been injected into the fracture by the time the crack height reaches $2a$. This means that at the end of the injection, the crack tip-line is approximately circular and $\tilde{v}_V$ should approximate the ascent velocity at this time. We expect that if the time scale of injection is much lower than the time scale of propagation, that once the crack has exceeded the critical radius of Davis *et al.* (2020), it will begin to elongate in the direction of the stress gradient. In these cases, the upwards ascent speed should lie somewhere between the two limiting regimes; that predicted by equation (2.5) of a finite fluid batch, and the ascent rate defined by a constant fluid flux, equation 2.4 (Möri & Lecampion 2021*b*). Even when the injection rate is low, once the entire fluid batch has been injected into the fracture and as t increases, our analysis to predict the deceleration rate will remain valid. One example of this can be seen in the analog gelatin data in Fig. 5. Here, for M50 silicon oil the ascent rate doesn't reach $\tilde{v}_V$ because the injection rate was low. Despite this, our equation predicts the decay in the speed at later times.

Mutch *et al.* (2019) use geochemical techniques to retrieve magma ascent rates of the Borgarhraun eruption, northern Iceland. These results suggest the magma's ascent through the crust was rapid, in the range of 0.02 to 0.1 m s^{-1}. We now test to see if our equations can correctly predict such ascent speeds. The erupted lava volume of Borgarhraun was reported between 0.014–0.14 km^3 and the magma density was around 2700 kg m^{-3} (Maclennan *et al.* 2003; Hartley & Maclennan 2018). Assuming the following parameters: $\rho_r = 2750$ kg m^{-3}, $E = 10$–40 GPa, $\nu = 0.25$ and $\eta = 10$–30 Pa s, we find the maximum ascent rate from equation (3.4) between 0.08 and 9.4 m s^{-1}. Calculating the average speed from equation (3.6) between $2a$ and the reported distance traversed by the batch of 24 km, we find that it is between 0.06 and 9.6 m s^{-1}. Hence we observe that by using approximate crustal parameters, our analysis provides a simple means to predict and explain how a relatively small batch of magma can traverse the crust within a week.

Our results are also important in the context of hydro-fracturing operations. They can be used to quantify the time it would take for a fluid to pass into overlying formations and, furthermore, they give an estimate of the area of rock exposed to the crack surfaces. We aim here to give an indication of how this formula can be applied to industrial operations such as hydro-fracturing. We envision the case of injecting a fluid volume of 25 m^3, where the fluid viscosity ranges between 10^{-3}–10^{-2} Pa s, the rock stiffness's is 10–40 GPa and assuming the rock and fluid density are 2700 kg m^{-3} and 1000 kg m^{-3}, respectively. For this range of properties, using equation (3.5), it would take between 15 minutes to 5 hours for the fracture to propagate 1000 m vertically and 2 to 40 hours to propagate 2000 m, noting that for the faster ascent rates, turbulent flow may occur in the early stages of ascent. These ascent rates and distances suggest this is an efficient way to transport fluid through the crust, and they beg the question, which processes act to slow or stop this ascent? Low-viscosity fluids in porous formations can leak into the surrounding rock. This process is known as fluid leak-off, this would reduce the effective volume driving the fracture upwards and could, in some cases, change the dynamics of flow-driven fracture growth within the tip (Dontsov & Peirce 2015). Note, that in the context of a dyke, solidification of the magma along the dyke walls is mathematically equivalent to leak-off. This process is well understood for constant inflow 2D buoyant cracks (Lister 1994*b*). It is of interest to quantify how the upward propagation speed and trapping height for a finite volume of fluid is changed by fluid leak-off/solidification during ascent (Detournay 2004). Here we leave this extended analysis to future studies where more experimental data is available, but note that Lister (1994*a*,

489 Eq.5.1) provides a 2D approximation of the maximal distance a fixed finite-area dyke can
490 propagate when solidification is considered. Recall that in Sec. 3.2 we have shown how to
491 convert similar equations to 3D.

6. Conclusions

493 We have provided an analytical approximation of the maximum ascent speed of a three-
494 dimensional, buoyant fluid-driven fracture containing a finite fluid volume. We verified this
495 by comparison with outputs from a hydro-fracture simulator. We showed that the ascent speed
496 decays away from this maximum due to viscous drag in the growing tail region, at a rate
497 that is asymptotic to $t^{-2/3}$. Our quantitative approximations help to explain why a dyke can
498 traverse the crust in a time that is of order days. They also bring hydro-fracturing operations
499 into question, suggesting typical injection volumes should ascend through the crust unless
500 another process acts to trap the fracture or drain off fluid.

7. Acknowledgements

8. Declaration of Interests

509 The authors report no conflict of interest.

9. Data and codes

511 The codes use to produce the figures and run the PyFrac simulations are at: https://doi.
512 org/10.5281/zenodo.6669935. The data and movies of the gelatin experiments and data
513 from the PyFrac simulations are at: https://doi.org/10.5281/zenodo.6669974.

Appendix A. 2D similarity solutions - fixed finite-area

515 We restate the solutions of Roper & Lister (2007) in dimensional coordinates. The half height
516 of a Weertman crack is (Pollard & Muller 1976)

$$c_h = \left(\frac{K_c}{\Delta\gamma\sqrt{\pi}} \right)^{2/3}. \tag{A 1}$$

518 The head length is $2c_h$ and it's areal is

$$A_h = \frac{K_c^2(1-\nu)}{2\mu\Delta\gamma}. \tag{A 2}$$

520 If the initial crack area is A, then the tail area is $A_t = A - A_h$. Roper & Lister (2007) define
521 the fracture's entire tail length as

$$z_t^+ = \left(\frac{9A_t^2\Delta\gamma t}{16\eta} \right)^{1/3}. \tag{A 3}$$

The opening profile (wall separation) of the head (w_h) is

$$\frac{w_h}{2} = \frac{(1-\nu)K_c}{2\mu}\sqrt{\frac{c_h}{\pi}}\sqrt{1-\left(\frac{z_h}{c_h}\right)^2}\left(1+\frac{z_h}{c_h}\right), \qquad \text{(A 4)}$$

where z_h spans from $-c_h$ to c_h. The separation of the walls in the tail (w_t) is

$$\frac{w_t}{2} = \sqrt{\frac{\eta z_t}{\Delta\gamma t}}, \qquad \text{(A 5)}$$

where here z_t spans from 0 to z_t^+ (from the base of the crack to where this meets the head solution). The two solutions are then joined by moving z_h upwards and neglecting parts thinner than the top of the tail at the base of the head solution. We remind readers that here, the crack's centre at time $t = 0$ lies at $z = c_h$ (the injection point).

REFERENCES

CARTWRIGHT, J., KIRKHAM, C., FOSCHI, M., H, NEIL., RODRIGUEZ, K. & JAMES, D. 2021 Quantitative reconstruction of pore-pressure history in sedimentary basins using fluid escape pipes. *Geology* **49** (5), 576–580.

DAHM, T. 2000 On the shape and velocity of fluid-filled fractures in the earth. *Geophysical Journal International* **142** (1), 181–192.

DAS, S.B., JOUGHIN, I., BEHN, M.D., HOWAT, I.M., KING, M.A., LIZARRALDE, D. & BHATIA, M. 2008 Fracture propagation to the base of the greenland ice sheet during supraglacial lake drainage. *Science* **320** (5877), 778–781.

DAVIS, T., RIVALTA, E. & DAHM, T. 2020 Critical fluid injection volumes for uncontrolled fracture ascent. *Geophysical Research Letters* **47** (14), e2020GL087774.

DETOURNAY, E. 2004 Propagation regimes of fluid-driven fractures in impermeable rocks. *International Journal of Geomechanics* **4** (1), 35–45.

DONTSOV, E.V. & PEIRCE, A.P. 2015 A non-singular integral equation formulation to analyse multiscale behaviour in semi-infinite hydraulic fractures. *Journal of Fluid Mechanics* **781**.

EPA, US 2016 Hydraulic fracturing for oil and gas: Impacts from the hydraulic fracturing water cycle on drinking water resources in the united states. *Washington, DC: US Environmental Protection Agency, EPA/600/R-16/236F* .

GERMANOVICH, L.N., GARAGASH, D., MURDOCH, L.C. & ROBINOWITZ, M. 2014 Gravity-driven hydraulic fractures. In *AGU Fall Meeting Abstracts*, , vol. 2014, pp. H53C–0874.

HARTLEY, M. & MACLENNAN, J. 2018 Magmatic densities control erupted volumes in icelandic volcanic systems. *Frontiers in Earth Science* **6**, 29.

HEIMPEL, M. & OLSON, P. 1994 Buoyancy-driven fracture and magma transport through the lithosphere: models and experiments. In *International Geophysics*, , vol. 57, chap. 10, pp. 223–240. Elsevier.

LISTER, J.R. 1990 Buoyancy-driven fluid fracture: the effects of material toughness and of low-viscosity precursors. *Journal of Fluid Mechanics* **210**, 263–280.

LISTER, J.R. 1994*a* The solidification of buoyancy-driven flow in a flexible-walled channel. part 1. constant-volume release. *Journal of Fluid Mechanics* **272**, 21–44.

LISTER, J.R. 1994*b* The solidification of buoyancy-driven flow in a flexible-walled channel. part 2. continual release. *Journal of Fluid Mechanics* **272**, 45–66.

LISTER, J.R. & KERR, R.C. 1991 Fluid-mechanical models of crack propagation and their application to magma transport in dykes. *Journal of Geophysical Research: Solid Earth* **96** (B6), 10049–10077.

MACLENNAN, J., MCKENZIE, D., HILTON, F., GRONVÖLD, K. & SHIMIZU, N. 2003 Geochemical variability in a single flow from northern iceland. *Journal of Geophysical Research: Solid Earth* **108** (B1), ECV–4.

MAIR, R., BICKLE, M., GOODMAN, D., KOPPELMAN, B., ROBERTS, J., SELLEY, R., SHIPTON, Z., THOMAS, H., WALKER, A., WOODS, E. & YOUNGER, P. 2012 Shale gas extraction in the uk: a review of hydraulic fracturing. *Tech. Rep.*. Royal Society and Royal Academy of Engineering.

MÖRI, A & LECAMPION, B 2021*a* Arrest of a radial hydraulic fracture upon shut-in of the injection. *International Journal of Solids and Structures* **219**, 151–165.

Möri, A. & Lecampion, B. 2021*b* Limiting regimes of a three-dimensional buoyant hydraulic fracture emerging from a point source. In *AGU Fall Meeting 2021*.

Möri, A., Lecampion, B. & Zia, H. 2020 Fully-coupled 3d modelling of magmatic dike propagation-finite pulse release from a point source. *Tech. Rep.*. Copernicus Meetings.

Moukhtari, F.E., Lecampion, B. & Zia, H. 2020 Planar hydraulic fracture growth perpendicular to the isotropy plane in a transversely isotropic material. *Journal of the Mechanics and Physics of Solids* **137**, 103878.

Mutch, E.J.F., Maclennan, J., Shorttle, O., Edmonds, M. & Rudge, J.F. 2019 Rapid transcrustal magma movement under iceland. *Nature Geoscience* **12** (7), 569–574.

Okamoto, A. & Tsuchiya, N. 2009 Velocity of vertical fluid ascent within vein-forming fractures. *Geology* **37** (6), 563–566.

Peirce, A. 2015 Modeling multi-scale processes in hydraulic fracture propagation using the implicit level set algorithm. *Computer Methods in Applied Mechanics and Engineering* **283**, 881–908.

Peirce, A. 2016 Implicit level set algorithms for modelling hydraulic fracture propagation. *Philosophical Transactions of the Royal Society A: Mathematical, Physical and Engineering Sciences* **374** (2078), 20150423.

Pollard, D.D. & Muller, O.H. 1976 The effect of gradients in regional stress and magma pressure on the form of sheet intrusions in cross section. *Journal of Geophysical Research* **81** (5), 975–984.

Pollard, D.D. & Townsend, M.R. 2018 Fluid-filled fractures in earth's lithosphere: Gravitational loading, interpenetration, and stable height of dikes and veins. *Journal of Structural Geology* **109**, 38–54.

Rivalta, E. & Dahm, T. 2006 Acceleration of buoyancy-driven fractures and magmatic dikes beneath the free surface. *Geophysical Journal International* **166** (3), 1424–1439.

Rivalta, E., Taisne, B., Bunger, A.P. & Katz, R.F. 2015 A review of mechanical models of dike propagation: Schools of thought, results and future directions. *Tectonophysics* **638**, 1–42.

Roper, S.M. & Lister, J.R. 2007 Buoyancy-driven crack propagation: the limit of large fracture toughness. *Journal of Fluid Mechanics* **580**, 359–380.

Rubin, A.M. 1995 Propagation of magma-filled cracks. *Annual Review of Earth and Planetary Sciences* **23** (1), 287–336.

Salimzadeh, S., Zimmerman, R.W. & Khalili, N. 2020 Gravity hydraulic fracturing: A method to create self-driven fractures. *Geophysical Research Letters* p. e2020GL087563.

Schultz, R.A. 2016 Causes and mitigation strategies of surface hydrocarbon leaks at heavy-oil fields: examples from alberta and california. *Petroleum Geoscience* **23** (2), 231–237.

Secor, D.T. & Pollard, D.D. 1975 On the stability of open hydraulic fractures in the earth's crust. *Geophysical Research Letters* **2** (11), 510–513.

Smittarello, D. 2019 Propagation des intrusions basaltiques. PhD thesis, Université Grenoble Alpes.

Smittarello, D., Pinel, V., Maccaferri, F., Furst, S., Rivalta, E. & Cayol, V. 2021 Characterizing the physical properties of gelatin, a classic analog for the brittle elastic crust, insight from numerical modeling. *Tectonophysics* **812**, 228901.

Spence, D.A. & Turcotte, D.L. 1990 Buoyancy-driven magma fracture: A mechanism for ascent through the lithosphere and the emplacement of diamonds. *Journal of Geophysical Research: Solid Earth* **95** (B4), 5133–5139.

Stevens, L.A., Behn, M.D., McGuire, J.J., Das, S.B., Joughin, I., Herring, T., Shean, D.E. & King, M.A. 2015 Greenland supraglacial lake drainages triggered by hydrologically induced basal slip. *Nature* **522** (7554), 73–76.

Tada, H., Paris, P. & Irwin, G.R. 2000 *The Stress Analysis of Cracks Handbook; Third edition*, , vol. 130. New York: ASME Press.

Taisne, B. & Tait, S. 2009 Eruption versus intrusion? arrest of propagation of constant volume, buoyant, liquid-filled cracks in an elastic, brittle host. *Journal of Geophysical Research: Solid Earth* **114** (B6).

Tolstoy, M., Cowen, J.P., Baker, E.T., Fornari, D.J., Rubin, K.H., Shank, T.M., Waldhauser, F., Bohnenstiehl, D.R., Forsyth, D.W., Holmes, R.C. & Love, B. 2006 A sea-floor spreading event captured by seismometers. *Science* **314** (5807), 1920–1922.

Weertman, J. 1971 Theory of water-filled crevasses in glaciers applied to vertical magma transport beneath oceanic ridges. *Journal of Geophysical Research* **76** (5), 1171–1183.

Zia, H. & Lecampion, B. 2020 Pyfrac: A planar 3d hydraulic fracture simulator. *Computer Physics Communications* **255** (107368), 1–11.

Zia, H., Lecampion, B. & Zhang, W. 2018 Impact of the anisotropy of fracture toughness on the propagation of planar 3d hydraulic fracture. *International Journal of Fracture* **211** (1), 103–123.